Assessment of statistical and hybrid LES turbulence closures for surface combatant DTMB5415 at 20° static drift condition

Michel Visonneau, Emmanuel Guilmineau, Jeroen Wackers, Ganbo Deng, Patrick Queutey

ASSESSMENT OF STATISTICAL AND HYBRID LES TURBULENCE CLOSURES FOR SURFACE COMBATANT DTMB5415 AT 20° STATIC DRIFT CONDITION

Michel Visonneau
Emmanuel Guilmineau
Jeroen Wackers
GanBo Deng
Patrick Queutey
LHEEA, CNRS UMR 6598
Ecole Centrale de Nantes, 1 rue de la Noë
BP 9210 44321 Nantes Cedex 3, France

ABSTRACT

This paper provides detailed validation of the complex free-surface flow around the surface combatant DTMB5415 at 20° static drift conditions. Particular emphasis is being placed on the onset and progression of the various vortical structures created at the sonar dome, at the free-surface and around bilge keels in conditions where free-surface breaking may occur. A detailed analysis of this complex free-surface flow is conducted on grids which are dynamically refined to capture the vortical structures. Local comparisons with recent experiments performed at the Iowa Institute of Hydraulic Research (IIHR) during a joint NATO-AVT (Advanced Vehicle Technologies) collaboration are used to perform detailed flow analysis and draw some conclusions about the actual potentialities of advanced Computation Fluid Dynamics (CFD) method in terms of physical and numerical modeling.

INTRODUCTION

The simulation of the onset and progression of longitudinal vortices is a major challenge in ship hydrodynamics because the accurate prediction of the flow in the core of vortices during their progression is strongly affected by numerical and turbulence modeling errors. This is however a topic of great practical importance since elongated bodies like ships give rise to various longitudinal vortices emanating from bulbous bows, sonar domes, hull-struts junctions, for instance. The accurate prediction of these flow structures and their trajectories can be crucial for global force prediction but also for the design of propellers when they interact with the propeller disk.

During the Gothenburg 2010 workshop, the calm water straight-ahead condition was studied in [1]. The low Froude number Fr = 0.142 large block coefficient Cb = 0.81 tanker hull forms (KVLCC2) and the higher Fr smaller Cb = 0.51 surface combatant DTMB5415 were chosen as test cases and used to assess in great detail the respective influence of discretization and modeling errors on the generation and progression of longitudinal vortices. For the KVLCC2, it was established that statistical anisotropic turbulence closures were still the best models to predict the generation of longitudinal vortices occuring in the aft part of the ship through the progressive thickening of the boundary layer. Hybrid Large-Eddy Simulation (LES) approaches, because of unphysical management of the turbulence production between the Reynolds-Averaged Navier-Stokes Equations (RANSE) domain and the pure LES region, were not able to generate enough turbulence in the LES region, leading to much too intense longitudinal vortices.

For the DTMB 5415, it appeared that the onset of vortical structures was highly dependent on the local grid fineness around the sonar dome. Actually, with a very fine grid built with the help of an automatic grid refinement (AGR) procedure, it was possible to predict the onset of all the vortical structures visible in detailed experiments without any significant influence of the turbulence

closures. However, once generated, the progression of these longitudinal structures was found to be highly dependent on the turbulence closures, even if a sufficiently fine grid was kept in the core of the vortices, thanks to the AGR procedure used with ad-hoc criterion. None of the above-mentionned closures (i.e. anisotropic statistical turbulence closures or DES model (also called hybrid LES closure)) were fully satisfactory, the statistical closures creating too much turbulence viscosity while DES did not generate enough turbuence in the core of the vortices. The reader can refer to [2] for more details on this topic.

The work presented in this study was performed during a collaborative project with NATO and partner countries under the auspices of the NATO AVT-183 Reliable Prediction of Separated Flow and Onset and Progression for Air and Sea Vehicles. The objective of this collaborative study is to present a first assessment of the DTMB5415 for the 20° static drift condition, including analysis of the turbulence modeling, grid resolution and onset and progression of vortex structures. Some of the salient results will be provided in this paper.

EXPERIMENTAL MODEL AND DATA

The experimental data used herein for 5415 with bilge keels at Fr=0.28 at static drift 20° condition is comprised of resistance and moments, wave elevation and profiles, flow and vorticity contours at several planes along the hull and isosurfaces of vorticity or velocity-gradient tensor invariant at selected 3D volumes along the primary vortices ([3], [4], [5]). The hull form used in the tests was the DTMB 5512, a 1:46.6 scale, 3.048 m long model, which is a geosym of the DTMB 5415, a 1:24.8 scale, 5.72 m model. The full-scale hull form is a preliminary design for a surface combatant for the US Navy. Characteristic features of the DTMB 5415 hull include a transom stern and a sonar dome bow. The model was un-appended except for bilge-keels, i.e., not equipped with shafts, struts, propellers, nor rudders (see Figure 1). The ship model was tested at three static drift angles $\beta = 0°$, $10°$ and $20°$, at a Fr = 0.28. This Froude number corresponds to the full-scale cruising speed of the vessel at 20 knots, and corresponds to 1.53 m/s for model scale. The model was fixed at its dynamic sinkage $\sigma = 1.92\ 10^{-3} L_{PP}$ and trim = $0.136°$ (bow down). Here L_{PP} is the length between perpendiculars. The tests were conducted in calm-water conditions.

CFD: THE ISIS-CFD FLOW SOLVER

The solver ISIS-CFD, available as a part of the FINE^{TM}/Marine computing suite, is an incompressible unsteady Reynolds-Averaged Navier-Stokes (URANS) solver mainly devoted to marine hydrodynamics. The discretization is based on a fully unstructured face-based finite volume method to build the spatial discretization of the transport equations. Pressure-velocity coupling is enforced through a Rhie & Chow SIMPLE type method: at each time step, the velocity updates come from the momentum equations and the pressure is given by the mass conservation law, transformed into a pressure equation. The method features several sophisticated turbulence models: apart from the classical two-equation $k-\varepsilon$ and $k-\omega$ models, the anisotropic two-equation Explicit Algebraic Stress Model (EASM), as well as Reynolds Stress Transport Models, are available [6, 7] with or without rotation corrections. All models are available with wall-function or low-Reynolds near wall formulations. Hybrid LES turbulence models based on Detached Eddy Simulation (DES and variants) are also implemented and are validated on automotive flows characterized by large separations (see [8]). Additionally, several cavitation models are available in the code. Free-surface flow is simulated with a multi-phase flow approach: the water surface is captured with a conservation equation for the volume fraction of water, discretized with specific compressive discretization schemes [9]. Finally, a parallelized anisotropic automatic grid refinement procedure has been developed which is controlled by various flow-related criteria [10].

FIGURE 1. DTMB5415 MODEL

RESULTS AT 20° DRIFT ANGLE

Settings

Two unstructured grids have been generated with HEXPRESS^{TM} without taking into account the presence of the tank walls. The first one, called here G1, is comprised of 27 million nodes while the second one is dynamically refined during the computations with the AGR procedure included in ISIS-CFD. This grid called G2 comprises only 10 million nodes. The automatic grid refinement used to create it is based on an hybrid criterion blending a free-surface and a vortex capturing criteria built with the regularized Hessian of the pressure. The minimum cell size is set at 2 mm for a ship length of 3.048m. Although these grids are still too coarse to capture accurately the progression of all the longitudinal vortices generated at the sonar dome and behind the breaking wave, along the entire hull and below the free-surface, these simulations can be used with confidence to assess the need in terms of discretisation and turbulence modeling in the vicinity of their region of onset. Figures 2 and 3 compare the grid density between G1 and G2 at two cross-sections in the fore region. Directional and anisotropic

adaptation is noticeable at the first section, Figure 2, associated with strong air/water interface deformations due to the high drift condition. In that section refinement has been created also at the vicinity of the sonar dome surface to be correlated with the presence of high pressure gradients. In the second section, Figure 3, a significant vortical structure on starboard side has developed which is illustrated by a localised region of refined grid with smaller cell sizes than provided with the fine grid.

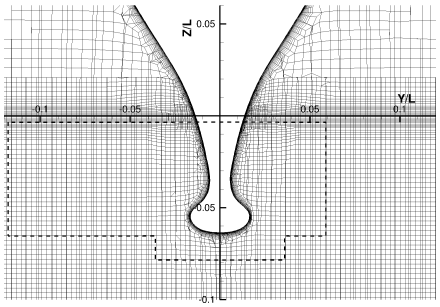

(a) FINE (G1)

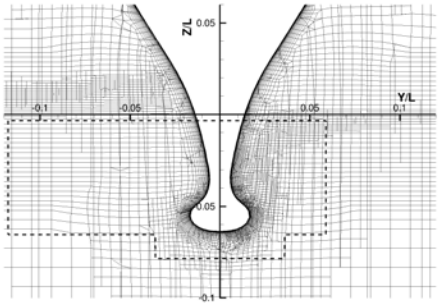

(b) AGR (G2)

FIGURE 2. GRID TOPOLOGY AT X/L_{PP}=0.06

Three different turbulence models are used, $k-\omega$ SST, EARSM and DES-SST, for the computations performed on grid G1. For the grid G2 built with AGR, only the $k-\omega$ SST model has been employed.

Forces

The agreement on the forces and moments shown in Tab. 1 is quite satisfactory for all the turbulence models and grids used. For the resistance, the best agreement is obtained with $k-\omega$ SST on the grid built with AGR with a comparison error of -0.35%D while the worst result is given by EARSM on the fine grid with a comparison error of 5.17%D. For the lateral force, the best agreement is reached by DES-SST on grid G1 with a comparison error

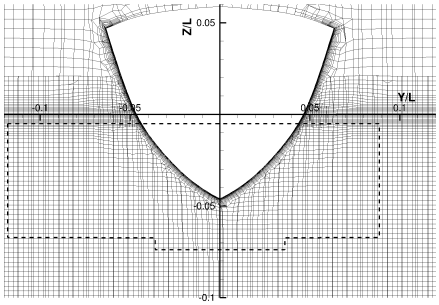

(a) FINE (G1)

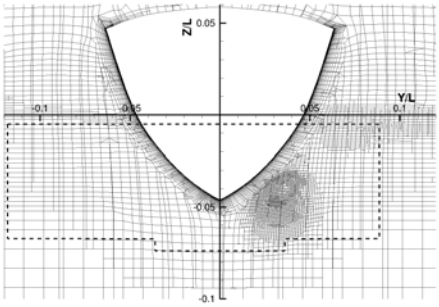

(b) AGR (G2)

FIGURE 3. GRID TOPOLOGY AT X/L_{PP}=0.20

of -0.22%D while the maximum error is 4.16%D for $k-\omega$ SST on grid G2. Finally, for the moment N, the best agreement with the measured value is provided by $k-\omega$ SST on grid G2 with a maximum error of -1.93%D obtained with the model EARSM on grid G1.

Wave elevations

Figure 4 shows the mean wave elevations for URANSE and DES-SST results on the grids G1 and G2. The wave patterns are globally very similar. An asymmetric wave elevation distribution is observed where two waves are generated from the bow, with angle 10° from the windward side (portside) and 40° from the leeward side (starboard). A strong breaking wave, with a large wave trough reaching the vicinity of the sonar dome, can be noticed on the leeward side (see figure 5). This wave trough is unsteady with a periodic growth and shrinkage of moderate amplitude, which means that the wave trough never disappears. This free-surface unsteadiness leads to a periodic temporal evolution of the wall streamlines below the free-surface close to this location. A second weaker shoulder wave can also be observed on the leeward side. On the windward side, a relatively weaker diverging wave emanates from the bow beginning with a wave crest.

TABLE 1. COMPARISONS OF FORCES BETWEEN CFD AND EFD. E%D=(S-D)/D*100

Case	X$\times 10^{-3}$ – E%D	Y$\times 10^{-3}$ – E%D	N$\times 10^{-3}$ – E%D
EFD	-28.57 –	153.57 –	59.86 –
URANS+AGR, $k-\omega$ SST (G2 - 10M)	-28.47 – -0.35	159.95 – 4.16	59.97 – 0.18
URANS, $k-\omega$ SST (G1 - 27M)	-29.01 – 1.54	155.68 – 1.38	58.91 – -1.58
URANS, EARSM (G1 - 27M)	-30.05 – 5.17	154.98 – 0.92	58.71 – -1.93
DES (G1 - 27M)	-28.06 – -0.35	153.24 – -0.22	60.88 – 1.70

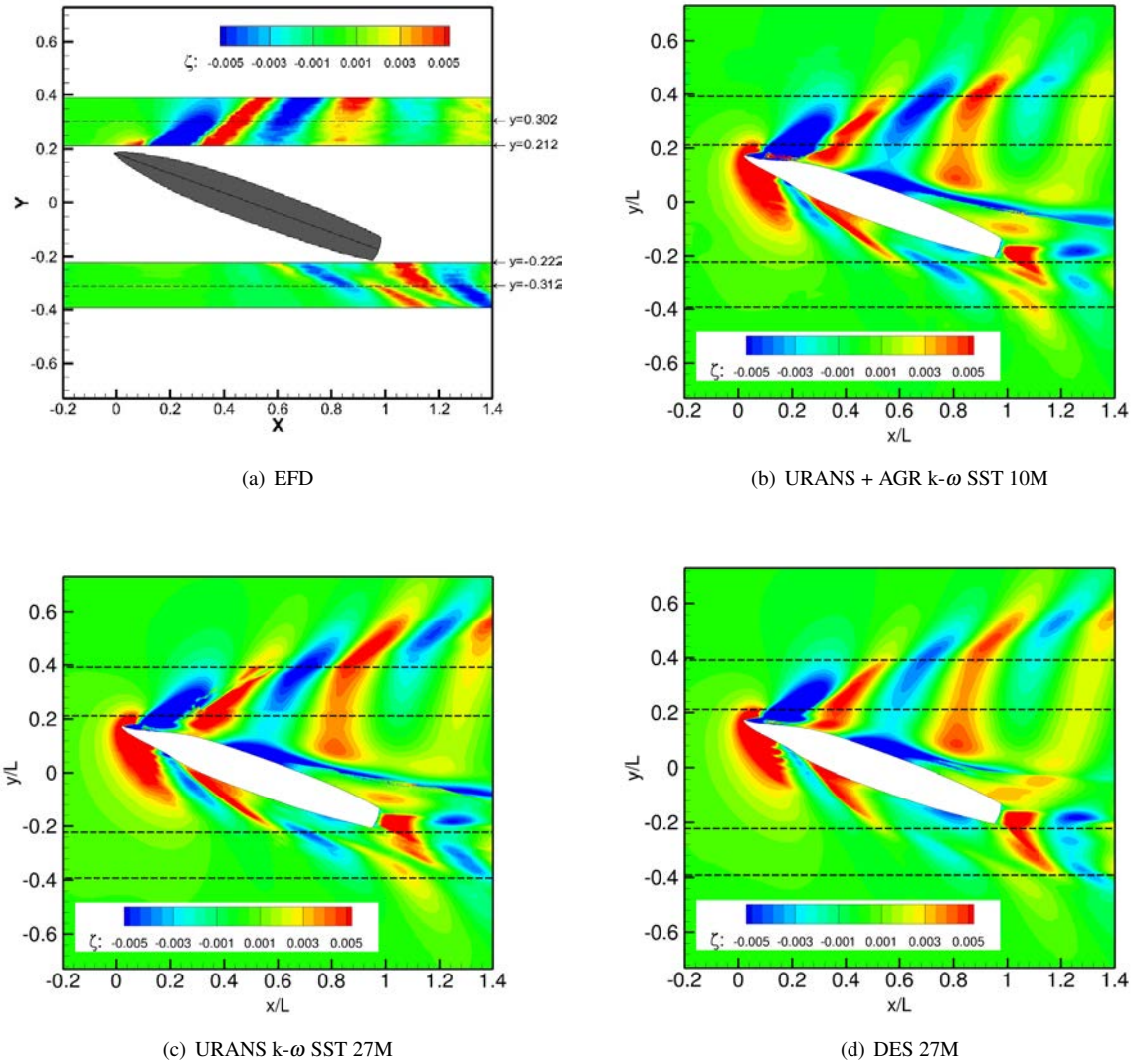

(a) EFD

(b) URANS + AGR k-ω SST 10M

(c) URANS k-ω SST 27M

(d) DES 27M

FIGURE 4. EFD AND CFD WAVE CONTOURS

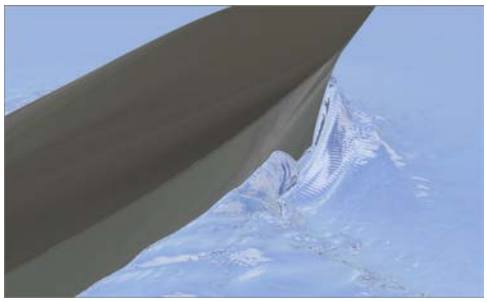

FIGURE 5. INSTANTANEOUS VIEW OF THE BREAKING WAVE ON THE LEEWARD SIDE

The simulated and measured wave profiles at $y_{ship} = -0.222$ on portside and $y_{ship} = 0.212$ on starboard side are shown in figures 6. The global agreement is quite satisfactory, considering the complexity of the wave profiles. A slight influence of the turbulence model and local grid density on the free-surface elevations can be noticed but it is difficult to draw any reliable conclusions on the basis of these fragmented comparisons.

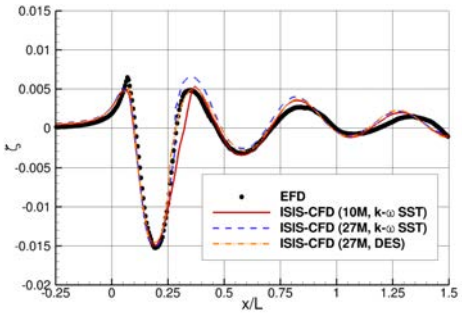

(a) At $y_{ship} = 0.212$ on SB side

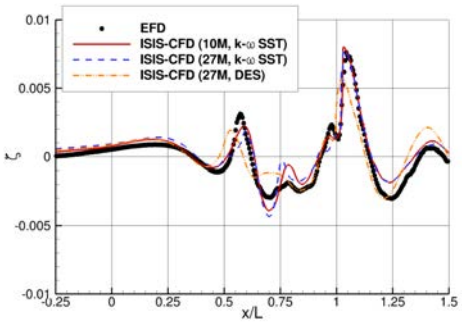

(b) At $y_{ship} = -0.222$ on PS side

FIGURE 6. EFD AND CFD WAVE PROFILES

Mean vortical structures

During the NATO/AVT joint collaboration, IIHR proposed a classification of mean vortex structures observed in this configuration by drawing the iso-surfaces Q=50 colored by the helicity. This terminology is retained in the present paper and shown in Figure 7(a). For a drift angle of 20°, the free-surface deformation is very large and leads to wave breaking and ventilation phenomena which are accompanied by the generation of two intense free-surface vortices (FSV) on the windward and leeward sides. These vortices, named by IIHR, LW-FSV and WW-FSV, originate from x/L_{PP} = 0.013 and progress towards the free-surface where they are associated with significant free-surface deformation. LW-FSV appears more intense and extends up to x/L_{PP} = 0.190 while WW-FSV extends up to x/L_{PP} = 0.217. From the sonar dome, three different vortices can be observed. The first and more intense one emanates from the leeward side of the sonar dome and is called Sonar Dome Tip Vortex (SDTV) by IIHR. Its extension varies according to the turbulence models (up to x/L_{PP} = 1.677 for EARSM and x/L_{PP} = 1.744 for DES-SST). An additional vortex, named Leeward ForeBody Keel Vortex (FBKV-LW), counter rotating to SDTV, is generated at the extremity of the sonar dome keel while its counterpart named WindWard ForeBody Keel Vortex (FBKV-WW), co-rotating with SDTV, is also visible in all the computations performed with every turbulence model on grids G1 or G2. The extension of these two vortices is more limited (up to x/L_{PP} = 0.431) where they are probably erased by the numerical diffusion. The analysis of the flow on the leeward side of the bow of the ship is far more complex. We notice the existence of a region of separated flow which is slightly unsteady because of the strong interactions of the separated flow with an unsteady breaking wave. The surface streamlines indicate the presence of a spiral point, whatever the turbulence closure used (see Figure 8). From these spiraling wall streamlines emerges a strong helical vortex convected below the free surface. This vortical structure is unsteady, periodically growing and shrinking in time and correlated with a similar unsteadiness of the leeward breaking wave. Around the bilge keels on the leeward side, two to three vortices are also visible starting from the leading edge, the middle part and the trailing edge of the leeward bilge keel. Their intensity is moderate like their spatial extension. They are all called bilge keel vortices (BKV). From the windward side, far more intense vortices (called BKTV vortices) are generated at the windward bilge keel. It seems that we can distinguish two such BKTV vortices, one of them having a large spatial extension since it moves below the hull and interacts up to x/L_{PP}=1.690.

Onset and progression analysis of SDTV

Figures 10 show the longitudinal evolution of several physical variables in the SDTV vortex cores. To identify the vortex cores, we have launched a streamline from the onset point identi-

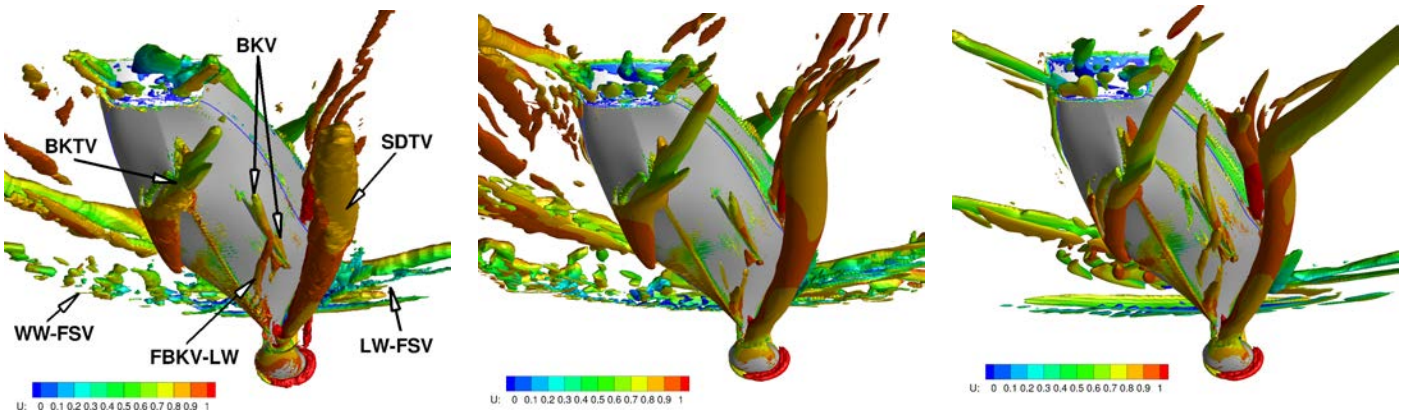

(a) URANS + AGR k-ω SST 10M (b) URANS k-ω SST 27M (c) DES 27M

FIGURE 7. ISO-SURFACES OF Q=50 COLORED BY RELATIVE HELICITY

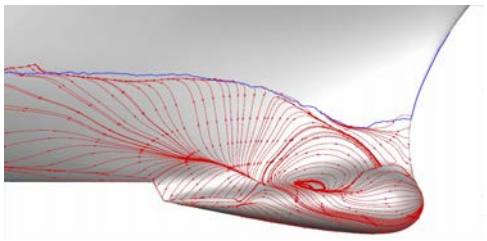

FIGURE 8. INSTANTANEOUS WALL STREAMLINES TOPOLOGY ON THE LEEWARD SIDE OF THE SONAR DOME

fied with great care and have recorded the longitudinal evolution of these variables at several locations along this line. This explains why we have data in the region where the SDTV vortex is no more detected by the iso-surface Q=50. However, this does not mean that the vortex has been completely diffused here but, rather, that its intensity is weaker, leading to Q value positive but smaller than 50. This was checked by drawing the secondary velocities in a plane normal to the vortex line, confirming the existence of a transverse rotational motion. Figures 10 showing Q_{peak} and axial vorticity ω_x confirm that the intensity of SDTV is strongly under-predicted, whatever turbulence closures used. For instance, ω_x is twice less intense in the computations than in the experiments, which points out the lack of grid points in this specific region. The prediction of ω_y and ω_z is somewhat better, whatever turbulence closures used. The trajectory of SDTV is remarkably well predicted since we can observe an almost perfect agreement between computations and measurements of Y and Z evolutions along the SDTV vortex core. The evolution of the longitudinal velocity component Ux is better predicted with the AGR 10M points grid and is somewhat under-predicted on the 27M points grid, underlining again the role played by the local discretization error for this kind of flow. The turbulent kinetic energy (TKE) appears also to be strongly under-predicted in every computation.

Planar Variables

EFD data are available for comparisons with CFD at x/L_{PP} =0.06, 0.1, 0.12, 0.2, 0.4, 0.6, 0.8, 0.935 and 1.0. Data concerns axial velocity, cross flow streamlines, vorticity and TKE contours. For the sake of brevity, only planes 0.06 and 0.20 are shown and discussed in this paper. At x/L_{PP}=0.06, Figure 11 for vorticity component and Figure 12 for TKE, the flow is predicted similarly by URANSE and DES-SST computations. However, but not shown here, it is interesting to mention that DES-SST is the only model able to exhibit a significant amount of TKE from x/L_{PP}=0.02 to x/L_{PP}=0.035, coming exclusively from the resolved part of the turbulence. This resolved turbulence may come from the turbulence locally created by the impact of the breaking wave. This hypothesis will be studied further to provide an explanation of the large disagreement between the predicted and measured turbulence kinetic energy in the core of SDTV. This resolved TKE is very quickly diffused and is hardly detected at the first experimental cross section x/L_{PP}=0.06, Figure 12.

At x/L_{PP}=0.20, we can follow the progression of the most significant vortex, the so-called sonar-dome tip vortex (SDTV). In addition, we can notice the birth of an additional vortex close to the hull (probably FBKV-LW) The main source of disagreement between CFD and EFD concerns the level of TKE in the core of SDTV. All the predictions on fine grid G1 fail to capture the right amount of TKE while the computations on AGR grid G2 show a better trend. It is quite interesting to notice that DES-SST computed on G1 does not bring any significant improvement for this configuration.

In conclusion, before x/L_{PP}=0.10, the grid density seems to be high enough to capture the relevant physics in the flow do-

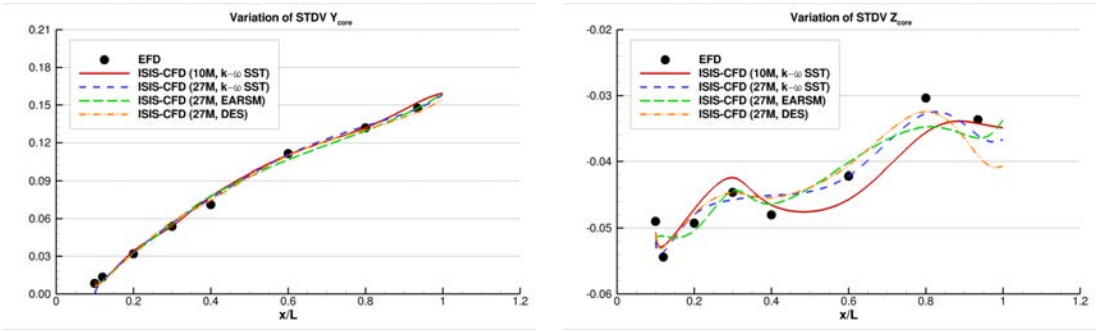

(a) Location Y_{core} (b) Location Z_{core}

FIGURE 9. EFD CFD LOCATION OF THE SDTV CORE VORTEX

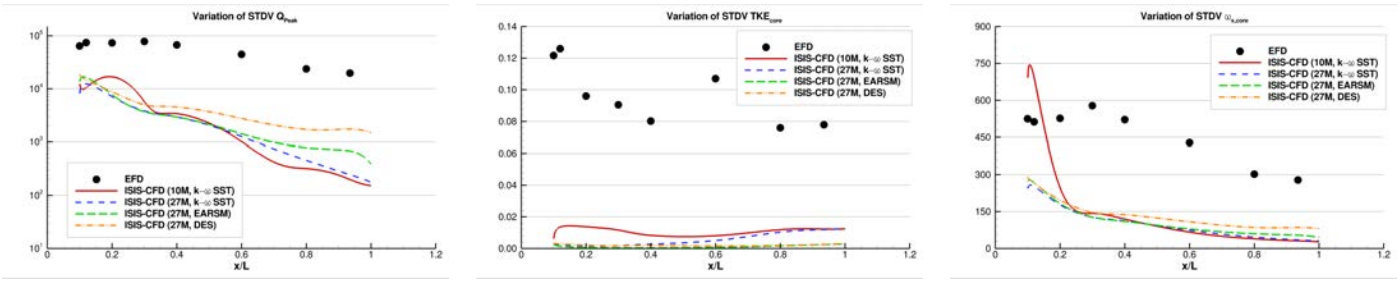

(a) Q_{peak} (b) TKE_{core} (c) $\omega_{x,core}$

FIGURE 10. EFD AND CFD VARIABLES IN SDTV CORE VORTEX

main. However, the grid is probably too coarse to capture the gradients and temporal scales of a flow associated with an unsteady free-surface breaking wave on the leeward side. All turbulence closures provide very similar predictions in the flow domain and the differences are observed only on the free-surface shape, depending on the extent of the air cavity in the predicted breaking wave. After x/L_{PP}=0.10, the grids used in this study appear too coarse as it is suggested by the large difference observed between results on G1(fine) and G2(AGR). It seems that after this section, a major source of error comes from the discretization since the turbulence closures provide very similar results on the same grid G1, which can not be considered as ridiculously coarse. However, it is noteworthy to look at the level of TKE measured at this section. It seems that SDTV emanates from a region where a large production of TKE takes place. This high level of TKE present in the core of the vortex is then convected in the flow domain without being significantly reduced. Measurement at x/L_{PP}=0.06 points out also a high level of TKE approximately in the region where SDTV comes to life. This region is very close to the highly deformed free-surface characterized by a strong breaking wave and large air-cavity. It is possible that the source of this high level of TKE has to be found in the interactions between the flow and the free-surface, where a strong production of turbulence might first take place, the turbulence being convected in the core of the SDTV vortex if the grid is fine enough. A second hypothesis would be that the SDTV vortex is not perfectly steady but changes its position in time. The large velocity fluctuations associated with this unsteadiness might be interpreted as an additional source of TKE in the PIV experiments, while they should be attributed to fluctuations in position of the core of the vortex. An other source of error might be attributed to a partial air ventilation and subsequent convection of bubbles of air inside the core of this vortex, which may disturb the measurements.

Anyway, this would plead in favor of a very fine grid free-surface capturing LES computation able to capture spatial and temporal scales associated with the free-surface and also velocity fluctuations associated with the impact of breaking waves to explain the source of this high level of TKE. Therefore, to understand the real physics, it seems necessary (i) to recheck with great care these local measurements, (ii) to use a DES-SST model to resolve as much as possible the velocity fluctuations coming from the impact of the breaking wave and make the distincton between the resolved macro-fluctuations of the velocity and the modeled turbulence, (iii) to use a locally very fine grid in order to reduce as much as possible the numerical dissipation during the progres-

sion of these vortices.

CONCLUSIONS

This paper was devoted to global and local comparisons of the free-surface flow around the DTMB5415 at 20° steady drift condition. Detailed experiments were performed at IIHR and made available in the framework of the NATO/AVT183 collaboration. Two grids with and without automatic grid refinement and several statistical and hybrid LES turbulence closures, were used and compared. The global quantities like forces and moments are satisfactorily simulated and the simulated free-surface deformation is also in good agreement with the measurements. However, more experimental information would be necessary to understand the detailed dynamics of the wave-breaking occuring on both sides of the bow. The agreement on the onset and progression of the longitudinal vortices emananting from both sides of the sonar dome and from the breaking waves is only qualitative. Obviously, these computations on grids G1, and to a lesser extent for grid G2, suffer from too large a numerical dissipation, although the improvements brought by the the AGR procedure were shown. The main vortical structures visible in the three-dimensional experiments can be detected, sometimes with a good quantitative agreement. Surprisingly, the trajectories of the core of the two studied vortices SDTV and BKTV (not shown here), are in excellent agreement with IIHR measurements. However, the flow field in the core of these vortices, in terms of mean flow and turbulence, appears to be strongly damped, which makes impossible a reliable analysis of the modeling errors. An additional study with a far more refined mesh using the local automatic grid refinement functionalities implemented in ISIS-CFD should be pursued to clarify the respective predictive qualities of RANSE models versus hybrid LES closures.

ACKNOWLEDGMENT

Recent unpublished experiments performed by IIHR in the framework of the NATO/AVT183 collaboration have been used in this paper. Professor Frederick Stern and his team are gratefully acknowledged for this very helpful initiative.

The computations were performed using HPC resources from GENCI (Grand Equipement National de Calcul Intensif) (Grant2014-0129 and Grant2014-21308), which is gratefully acknowledged.

REFERENCES

[1] Larsson, L., Stern, F., and Visonneau, M., 2014. *Numerical Ship Hydrodynamics: An Assessment of the Gothenburg 2010 Workshop*. Springer.

[2] Visonneau, M., Guilmineau, E., Queutey, P., Wackers, J., and Deng, G., 2014. "Assessment of statistic and hybrid LES turbulence closures for complex free-surface flow simulation with combined grid refinement criteria". In Thirtieth Symposium on Naval Hydrodynamics.

[3] Yoon, H., Simonsen, C., Bouscasse, B., Longo, J., Toda, Y., and Stern, F., 2014. "Benchmark CFD validation data for surface combatant 5415 in PMM maneuvers - Part i: Force/moment/motion measurements". *Manuscript in preparation*.

[4] Yoon, H., Gui, L., Bhushan, S., and Stern, F., 2014. Tomographic PIV measurements for surface combatant 5415 straight ahead and static drift 10 and 20 degree conditions. IIHR report in preparation.

[5] Longo, J., Shao, J., Irvine, M., and Stern, F., 2007. "Phase-averaged PIV for the nominal wake of a surface ship in regular head waves". *ASME Journal of Fluids Engineering,* ***129***, pp. 524–540.

[6] Deng, G. B., and Visonneau, M., 1999. "Comparison of explicit algebraic stress models and second-order turbulence closures for steady flow around ships". In 7th Symposium on Numerical Ship Hydrodynamics, pp. 4.4–1–4.4–15.

[7] Duvigneau, R., Visonneau, M., and Deng, G. B., 2003. "On the role played by turbulence closures in hull ship optimization at model and full scale". *Journal of Marine Science and Technology,* ***8***, pp. 11–25.

[8] Guilmineau, E., Chikhaoui, O., Deng, G., and Visonneau, M., 2013. "Cross wind effects on a simplified car model by a DES approach". *Computers and Fluids,* ***78***, pp. 29–40.

[9] Queutey, P., and Visonneau, M., 2007. "An interface capturing method for free-surface hydrodynamic flows". *Computers and Fluids,* ***36***, pp. 1481–1510.

[10] Wackers, J., Deng, G. B., Leroyer, A., Queutey, P., and Visonneau, M., 2012. "Adaptive grid refinement for hydrodynamic flow simulation". *Computers & Fluids,* ***55***, pp. 85–100.

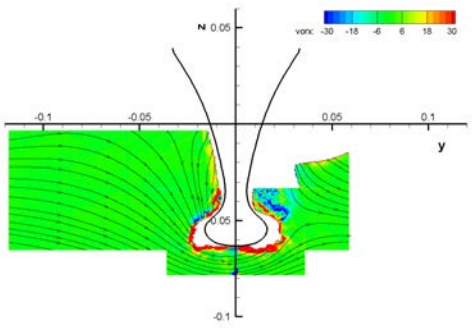

(a) EFD

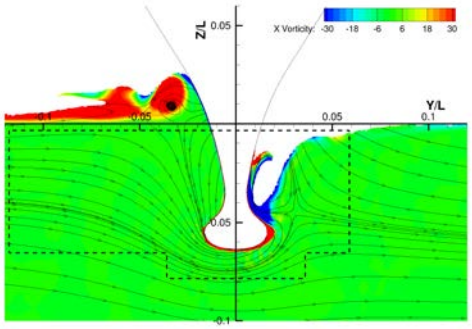

(b) URANS + AGR k-ω SST 10M

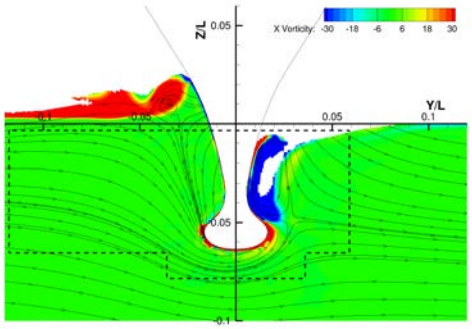

(c) URANS k-ω SST 27M

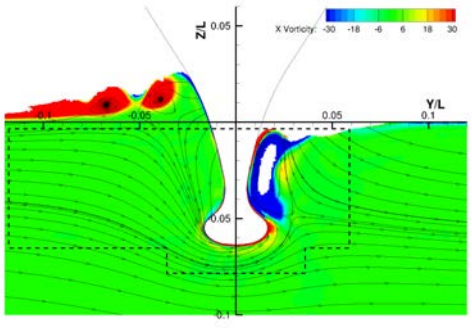

(d) DES 27M

FIGURE 11. CONTOURS OF AXIAL VORTICITY COMPONENT AT $X/L_{PP} = 0.06$

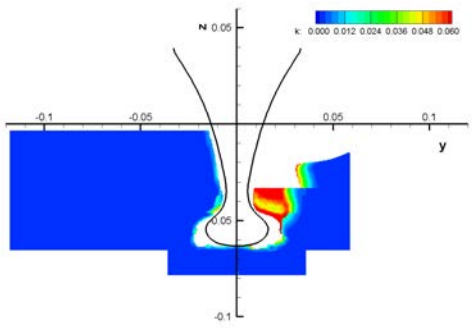

(a) EFD

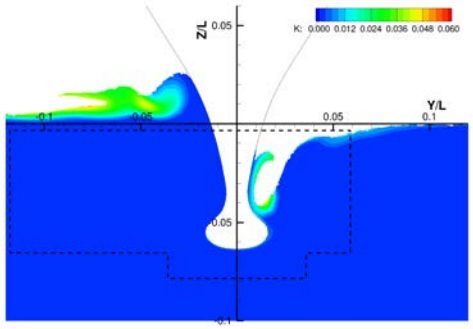

(b) URANS + AGR k-ω SST 10M

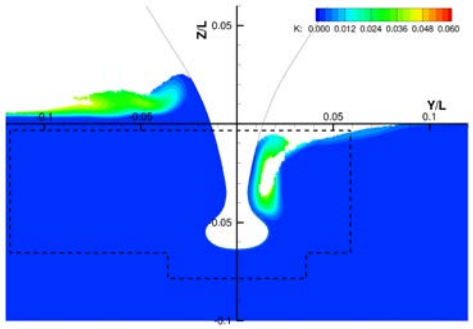

(c) URANS k-ω SST 27M

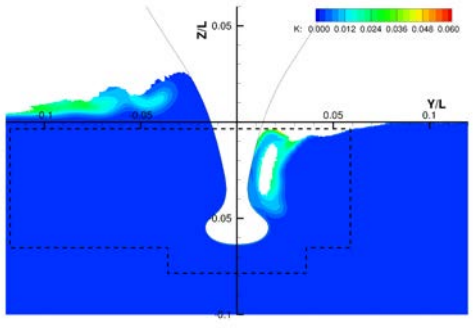

(d) DES 27M

FIGURE 12. CONTOURS OF TKE AT $X/L_{PP} = 0.06$

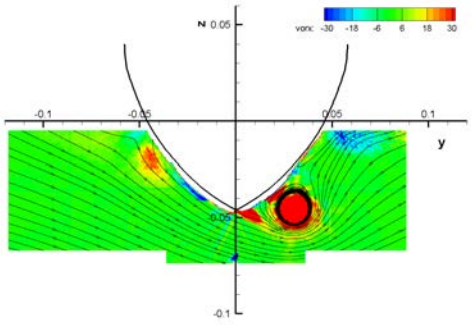

(a) EFD

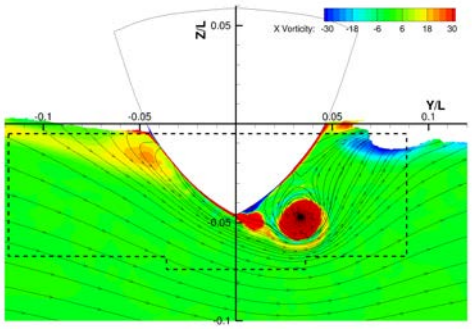

(b) URANS + AGR k-ω SST 10M

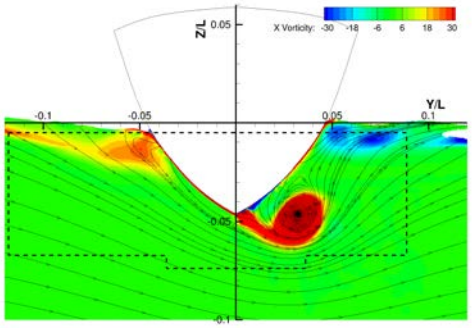

(c) URANS k-ω SST 27M

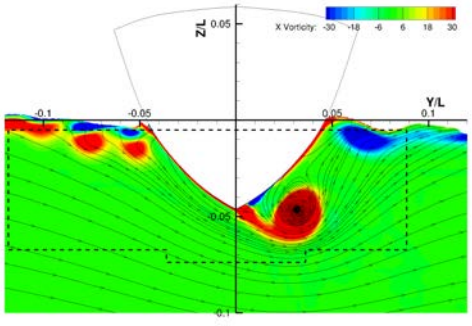

(d) DES 27M

FIGURE 13. CONTOURS OF AXIAL VORTICITY COMPONENT AT $X/L_{PP} = 0.20$

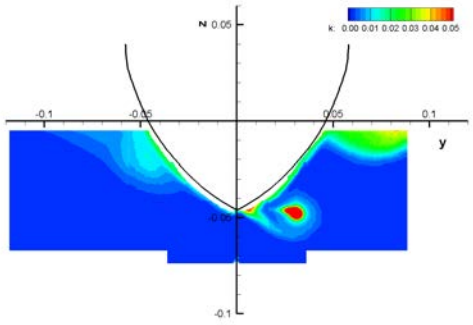

(a) EFD

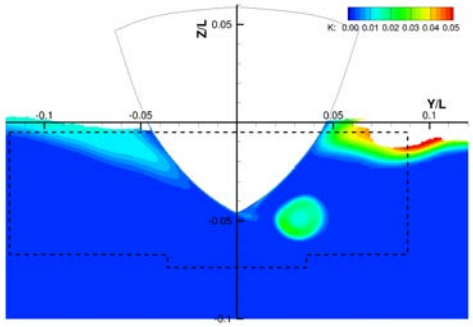

(b) URANS + AGR k-ω SST 10M

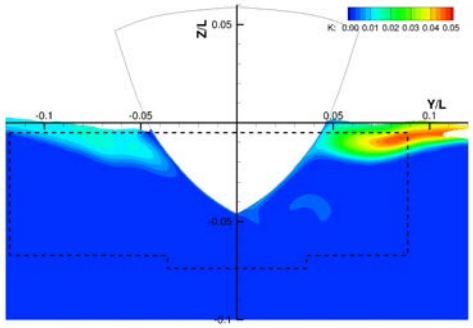

(c) URANS k-ω SST 27M

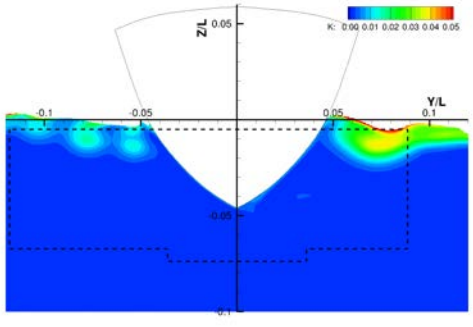

(d) DES 27M

FIGURE 14. CONTOURS OF TKE AT $X/L_{PP} = 0.20$